Inorganic Chemistry

Article

pubs.acs.org/IC

Structure and Magnetic Properties of $Cu_3Ni_2SbO_6$ and $Cu_3Co_2SbO_6$ Delafossites with Honeycomb Lattices

J. H. Roudebush,*[,†] N. H. Andersen,[‡] R. Ramlau,[§] V. O. Garlea,[∥] R. Toft-Petersen,[⊥] P. Norby,[#] R. Schneider,[▽] J. N. Hay,[†] and R. J. Cava[†]

[†]Department of Chemistry, Princeton University, Washington Road, Princeton, New Jersey 08544, United States

[‡]Department of Physics, Technical University of Denmark, DTU Risø Campus, Frederiksborgvej 399, Building 108-121-129-228, DK-4000 Roskilde, Denmark

[§]Max Planck Institute for Chemical Physics of Solids, Nöthnitzer Strasse 40, D-01187 Dresden, Germany

[∥]Quantum Condensed Matter Division, Oak Ridge National Laboratory, P.O. Box 2008, Oak Ridge, Tennessee 37831, United States

[⊥]Helmholtz Zentrum Berlin for Materials and Energy, Kekuléstrasse 5, D-14109 Berlin, Germany

[#]Materials Research Division, Technical University of Denmark, AFM-228, Frederiksborgvej 399, P.O. Box 49, DK-4000 Roskilde, Denmark

[▽]Laboratory for Electron Microscopy, Karlsruhe Institute of Technology, Engesserstrasse 7, Geb. 30.22 (Physik Flachbau), 2. OG, Zimmer 228, D-76128 Karlsruhe, Germany

Supporting Information

ABSTRACT: The crystal structures of two Delafossites, $Cu_3Ni_2SbO_6$ and $Cu_3Co_2SbO_6$, are determined by high-resolution synchrotron powder X-ray diffraction. The Ni and Co are ordered with respect to Sb in the layer of edge sharing octahedra, forming magnetic layers with honeycomb geometry. High-resolution electron microscopy confirms ordering, and selected-area electron diffraction patterns identify examples of the stacking polytypes. Low temperature synthetic treatments result in disordered stacking of the layers, but heating just below their melting points results in nearly fully ordered stacking variants. The major variant in both cases is a monoclinic distortion of a 6-layer Delafossite polytype, but a significant amount of a 2-layer polytype is also present for the Ni case. The antiferromagnetic ordering with transitions, at 22.3 and 18.5 K for Ni and Co variants, respectively, is investigated by temperature and field dependent magnetization, as well as specific heat. The sharp magnetic transitions support the presence of well developed 2:1 ordering of the Co:Sb or Ni:Sb ions in the honeycomb layers. Neutron diffraction measurements at 4 K are used to determine the magnetic structures. For both the Ni and Co phases, the propagation vector is $\mathbf{k} = [100]$, and can be described as alternating ferromagnetic chains in the metal-oxide plane giving an overall antiferromagntic "zigzag" alignment. While orientation of the magnetic moments of the Co is along the *b*-axis, the Ni moments are in the *ac* plane, approximately parallel to the stacking direction. Bulk magnetization properties are discussed in terms of their magnetic structures.

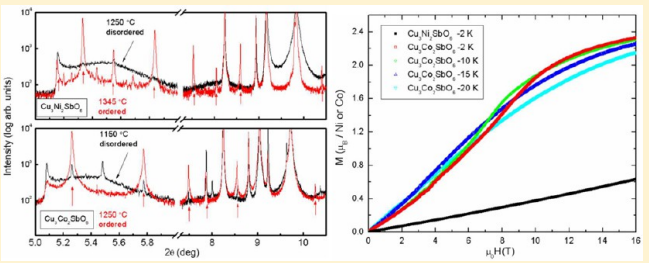

INTRODUCTION

The Delafossite ($CuFeO_2$) structure is formed from triangular layers of edge-sharing metal−oxygen octahedra separated by Cu^{1+} sticks; it is similar to the $NaFeO_2$ structure, with layers of Cu^{1+} sticks replacing the layers of Na^+ octahedra. Materials with the $CuFeO_2$ and $NaFeO_2$ structures have been of interest as transparent films with p-type conductivity,[1] thermoelectrics,[2] superconductors,[3] and multiferroics.[4] Two polytypes are commonly found for Delafossites: The "2*H*" 2-layer hexagonal polytype, in which the axes of the octahedra are oriented 180° in neighboring layers that are stacked in a hexagonal closed packed fashion, and the "3*R*" 3-layer rhombohedral polytype, in which all octahedra axes are oriented in the same direction, and the stacking is cubic close packed. These polytypes have also been recently referred to as D2 and D3, where "D" denotes the dumbbell configuration of Cu^{1+} and the number denotes the number of layers in the unit cell. In this work only a D2 polytype is observed.[5,6]

Formation of an ordered metal-oxide octahedral layer with a mix of magnetic and nonmagnetic atoms in a 2-to-1 ratio, i.e., $Cu_3B'_2B''O_6$ (where B′ and B″ can be transition or main group metals), results in the presence of a magnetic honeycomb lattice. Honeycomb lattices are not regarded as a magnetically frustrated geometry when only near neighbor interactions are considered. However, more complex magnetic properties have

Received: February 20, 2013

   dx.doi.org/10.1021/ic400415h | Inorg. Chem. XXXX, XXX, XXX−XXX

been found in materials such as Na_2IrO_3,[7,8] Cu_5SbO_6,[9] $Na_3Cu_2SbO_6$,[10] and $BaM_2(XO_4)_2$ for M = Ni, Co and X = P, As,[11] where higher order magnetic neighbor interactions are not negligible.

$Cu_3Ni_2SbO_6$ and $Cu_3Co_2SbO_6$ have been previously reported as $CuNi_{2/3}Sb_{1/3}O_2$ and $CuCo_{2/3}Sb_{1/3}O_2$.[12] Both compositions were reported as disordered Delafossites, in which the Ni (or Co) and Sb are randomly distributed on the same crystallographic site in the planes of metal−oxygen octahedra. The disordered samples were synthesized at 1000 °C in air; a mixture of 2*H* and 3*R* polytypes was reported for $Cu_3Ni_2SbO_6$ and a 2*H* polytype for $Cu_3Co_2SbO_6$. In the current work, samples were heated to higher temperatures, resulting in only 2*H*-like orientation of octahedra.

As temperature was systematically increased, the order within the planes of metal−oxygen octahedra became observable, as evidenced by the appearance of additional Bragg reflections in powder diffraction patterns that require indexing to a larger, ordered, Delafossite unit cell. Here we report the synthesis, structure, and magnetic properties of these Delafossites, which have magnetic honeycomb lattices.

EXPERIMENTAL SECTION

$Cu_3Ni_2SbO_6$ and $Cu_3Co_2SbO_6$ were synthesized by mixing CuO (99.7% Alfa Aesar), NiO (99% Alfa Aesar) or Co_3O_4 (99.7% Alfa Aesar), and Sb_2O_5 (99.998% Alfa Aesar) in stoichiometric metal ratios (3:2:1). The mixed powders (∼1 g) were pressed into pellets, placed on an alumina boat, and heated for 24 h at 800 °C in air, followed by sequential grindings and heatings in air for 12 h at 1000, 1275, 1300, 1315, 1330, 1345, and 1360 °C (M = Ni) and 1000, 1250, and 1260 °C (M = Co). The best examples of the ordered variants were obtained by pelletizing the powders and heating at final temperatures of 1345 or 1250 °C for 48 h for M = Ni and Co, respectively. The Ni compound is deep orange-red terracotta in color while the Co compound is a dark burgundy. Structural and magnetic data were collected on samples of the ordered and disordered variants, with the latter samples obtained at heating temperatures ∼100 °C below those of the ordered variants. $Cu_3Zn_2SbO_6$ was synthesized by heating CuO, ZnO, and Sb_2O_5 to 1150 °C.

Samples were initially characterized by laboratory powder X-ray diffraction (PXRD) using a Bruker D8 FOCUS (Cu Kα) diffractometer. High resolution powder diffraction data was collected at ambient temperature at the 11BM beamline at the Advanced Photon Source (APS) at Argonne National Laboratory. The structures were determined from the synchrotron diffraction (SXRD) patterns using the Rietveld method implemented in the FullProf program.[13] Peak shapes were fitted using the Thompson−Cox−Hastings pseudo-Voigt function while the background was set as a linear interpolation of fixed points.

Refinement of the SXRD data was completed in two steps: For step 1, instrumental zero shift and lattice parameters were refined, followed by a Lorentzian strain parameter. The effect of stacking faults in the patterns was accommodated by employing an *hkl*-dependent size broadening parameter. In step 2, atomic positions and overall thermal parameter B_{ov} are refined, as were Ni/Sb and Co/Sb site occupancies, constrained to the 2:1 compound formula. The refined site occupancies showed some apparent minor mixing of the ions due to the presence of the stacking faults, which are positionally averaged in the diffraction data. In the case of ordered $Cu_3Ni_2SbO_6$, two polytypes were identified in the sample. Rietveld refinements of each individual phase (with small amounts of NiO) were undertaken separately, and then combined in the final refinement where only their relative fractions were refined. In the case of $Cu_3Co_2SbO_6$ only one Delafossite polytype was identified in the ordered sample.

Selected-area electron diffraction (SAED), high-resolution transmission electron microscopy (HRTEM), and energy dispersive X-ray analysis (EDXS) were performed using a FEI Tecnai G^2-F30 electron microscope (C_S = 1.15 mm) operated at 300 kV accelerating voltage. Aberration-corrected HRTEM was performed with a FEI Titan^3 80−300, likewise operated at 300 kV. Along the ray path below the objective lens, the latter microscope is equipped with a correction-lens system for spherical and other aberrations — for short C_S image correction —which allows obtaining HRTEM images with an information limit of 0.08 nm. The C_S image corrector was used to minimize and determine the residual objective-lens aberrations on the basis of the procedure described by Uhlemann and Haider.[14] Both microscopes were equipped with a Gatan UltraScan 100 CCD camera. Samples were prepared by grinding under n-butanol and dropping onto a holey carbon film.

Magnetic susceptibility measurements were performed using a CRYOGENIC Ltd. Cryogen Free Measurement System (CFMS). The temperature dependent susceptibility between 2 and 300 K was measured on polycrystalline samples of weights between 50 and 250 mg. Susceptibility was defined as the magnetic moment, *M*, divided by the applied field (μ_oH) of 0.1 T, and normalized to Bohr magnetons per Tesla. *M* versus *B* curves were linear at all temperatures greater than the magnetic ordering temperatures, T_N, to applied fields higher than 1 T. Below the magnetic ordering temperatures, *M* versus *B* curves were taken from 0 to 16 T. Heat capacity (HC) measurements were performed using the heat relaxation method in a Quantum Design Physical Property Measurement System (PPMS) by affixing the sample to a sapphire platform using Apiezon N grease. The heat capacity of the sample holder with grease was measured separately and subtracted from the sample data to obtain the materials' specific heat between 2 and 250 K. The nonmagnetic structural analogue $Cu_3Zn_2SbO_6$ was synthesized,[12] and its heat capacity was measured, with the resulting data employed by subtraction to obtain the magnetic contribution to the HC for the Co and Ni compounds. The high temperature HC of each sample in the 225−250 K range was normalized to match that of the $Cu_3Zn_2SbO_6$ sample for the purposes of estimating the magnetic entropy.

Neutron powder-diffraction experiments were conducted using the HB2A diffractometer at the High Flux Isotope Reactor. Data were collected using the 1.538 and 2.41 Å wavelengths, produced by Ge[115] and Ge[113] reflections of a vertically focusing germanium wafer-stack monochromator. The beam collimation was 12′−21′−6′ from reactor to sample. The instrument is equipped with 44 ^{3}He detector tubes that were scanned to cover the total 2θ range of 5−150° in steps of 0.05°. More details about the HB2A instrument and data collection strategies can be found in ref 13.

Representational analysis was used to determinate the symmetry-allowed magnetic structures that can result from a second-order magnetic phase transition, given the crystal structure before the transition and the propagation vector of the magnetic ordering. These calculations were carried out using the program SARAh-Representational Analysis.[15] The decomposition of the magnetic representation Γ_{mag} in terms of the nonzero irreducible representations (IRs) of little group G_k of the wave-vector **k**, for each crystallographic site examined, and their associated basis vectors, ψ_n, are given in Table 5. The labeling of the propagation vector and the IRs follows the scheme used by Kovalev. The refinement of the magnetic structure was performed using FullProf Suite program.[13] Structure and magnetic figures were constructed using the program Vesta 3.[16]

RESULTS AND DISCUSSION

Structural Characterization. The PXRD pattern (λ = Cu Kα) of $Cu_3Ni_2SbO_6$ synthesized at 1000 °C can be indexed to a simple 2-layer Delafossite unit cell ($P6_3/mmc$, a = 3.06 Å, c = 11.51 Å). Reflections at 2θ values of 37.1° and 59.3° are significantly broadened, and there are very weak reflections near 2θ = 20° that are not indexed by this cell (Figure 1). When heated in air to higher temperatures, the broadened reflections narrow and new reflections at 20° and 22° emerge. Figure 1 shows the evolution of these two trends, with the insert focused on the region between 2θ = 19° and 23°. A similar trend was

dx.doi.org/10.1021/ic400415h | Inorg. Chem. XXXX, XXX, XXX−XXX

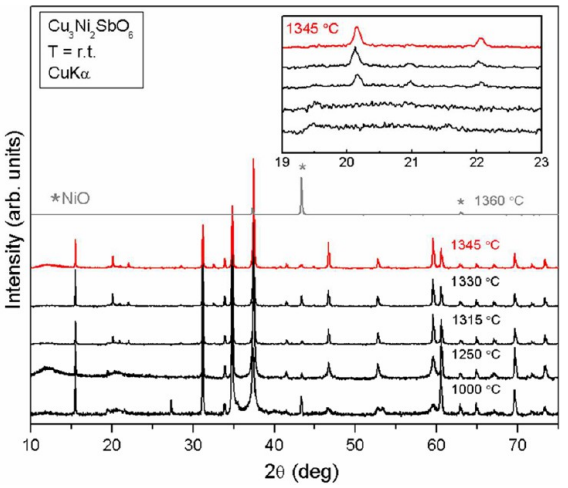

Figure 1. Laboratory powder X-ray diffraction patterns between 10° and 75° 2θ for $Cu_3Ni_2SbO_6$ samples heated in air at 1000, 1250, 1300, 1315, 1330, 1345, and 1360 °C. Peaks from NiO are clearly observed in the 1360 pattern and marked with a * symbol. Insert shows details of the diffraction pattern from 19° to 23° 2θ. Peaks related to the ordering of the Ni and Sb atoms emerge with increasing temperature.

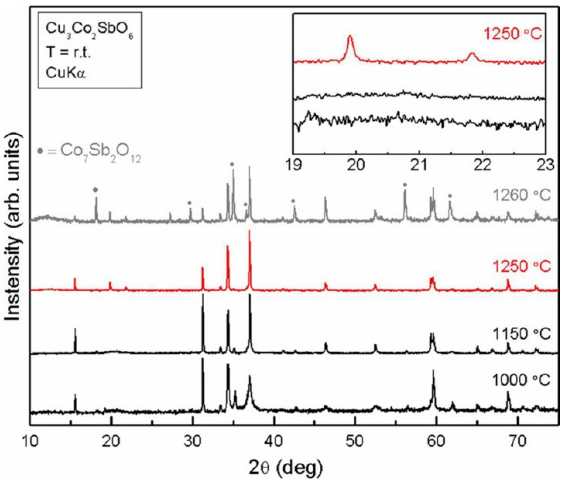

Figure 2. Laboratory powder X-ray diffraction patterns between 10° and 75° 2θ for $Cu_3Co_2SbO_6$ samples heated in air at 1000, 1150, 1250, and 1260 °C. The sample heated to 1260 °C has begun to decompose and peaks corresponding to a $(CoSb)_3O_4$ spinel, black ●, can be identified. The insert shows details from the patterns between 19° and 23° 2θ; the peaks at ~20° and 21° 2θ can be indexed to an ordered structure, with ordered Co and Sb atoms.

recently observed for Cu_5SbO_6,[9] where broadened reflections and weak low angle reflections were shown to be related to honeycomb layer ordering with stacking faults along the *c* axis. Upon heating the sample to 1360 °C, $Cu_3Ni_2SbO_6$ partially melts and only reflections corresponding to NiO are present in the remnant solid. To minimize the decomposition of the sample at temperatures just below the melting point, the sample was pelletized and covered with additional loose powder of its own composition. Comparison of the pelletized sample heated at 1345 °C to the loose powder heated at 1345 °C reveals that the partial decomposition, which is apparent from the appearance of NiO peaks, is reduced for the pelletized sample.

The PXRD patterns of the $Cu_3Co_2SbO_6$ sample display similar trends to those of the $Cu_3Ni_2SbO_6$ samples but with lower temperatures for formation of the ordered phase (1250 °C) and lower decomposition temperature (≤1260 °C); they are shown in Figure 2. Upon decomposition at 1260 °C, peaks corresponding to $(Co,Sb)_3O_4$ spinel dominate (cubic, a = ~8.56 Å). A method similar to that used for $Cu_3Ni_2SbO_6$ (see above) was used to minimize the decomposition of the sample at temperatures just below its melting point.

SXRD patterns (λ = 0.413 321 Å) were employed to compare the ordered and disordered samples and for structure determinations. Figure 3 compares the SXRD patterns for the ordered and disordered samples for both $Cu_3Ni_2SbO_6$ and $Cu_3Co_2SbO_6$. Examination of the 2θ region between 5−6° and 7.5−10.5° (equivalent to 19−23°, for λ = Cu Kα) reveals differences between the ordered and disordered samples and the presence of many low intensity peaks in the stacking fault region. These peaks typically have intensities of ~1000 counts while the greatest peak intensity observed in the sample is ~140 000 counts; therefore, this structural information was not available in the laboratory powder diffraction patterns.

For the $Cu_3Ni_2SbO_6$ sample (upper panel Figure 3) low intensity peaks marked with arrows in the stacking fault region, 2θ ~ 5−6°, and up to 10.5°, are evident in the ordered pattern but absent in the disordered one. There is also a clear difference in peak width between the ordered and disordered patterns; the

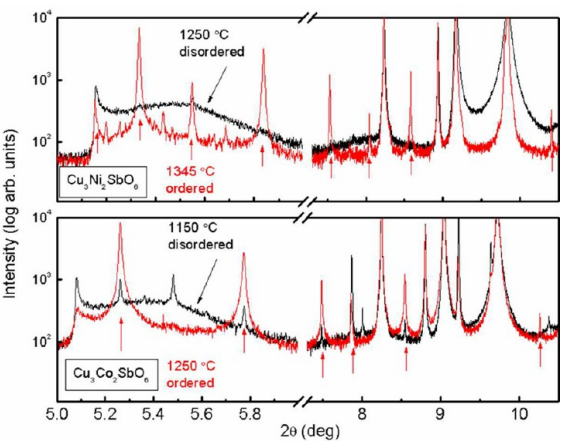

Figure 3. Comparison of high resolution synchrotron X-ray diffraction patterns for ordered and disordered $Cu_3M_2SbO_6$ samples; reflections associated with the M/Sb (M = Ni or Co) ordered structure ($C2/c$) are indicated with arrows. The top panel compares $Cu_3Ni_2SbO_6$ ordered (1345 °C, red line) and disordered (1250 °C, black line) samples. The bottom panel compares $Cu_3Co_2SbO_6$ ordered (1250 °C, red line) and disordered (1150 °C, black line).

reflection at 2θ ~ 9.75° gives one of the most severe examples. Peaks indexed to *hkl* Bragg reflections exhibit peak broadening, but those with an *hk0* or 00*l* index do not. The selective peak broadening can be attributed to the presence of stacking faults, i.e., disruptions of the regular stacking of one *ab* plane relative to another, and is common in Delafossite structures.[17,18]

For $Cu_3Co_2SbO_6$ (lower panel Figure 3), the differences between ordered and disordered samples is less striking than for the $Cu_3Ni_2SbO_6$ samples. Examination of the stacking fault region reveals that the ordered sample has two large reflections at ~5.25° and 5.75° 2θ while the disordered sample has two additional reflections of lesser intensity at ~5.1° and 5.5° as well as reflections at 5.25° and 5.75°. This suggests that both samples are "ordered"; however, the reflections from the sample heated to 1250 °C are of greater intensity and could be

dx.doi.org/10.1021/ic400415h | Inorg. Chem. XXXX, XXX, XXX−XXX

observed in the laboratory PXRD pattern (Figure 2). The additional peaks at 5.1° and 5.8° 2θ are similar to those found for the 2*H* polytype in the Ni sample (see below); therefore, it is possible that the Co heated to 1150 °C contains two polytypes. The peak widths are similar for both the ordered and disordered samples suggesting that stacking faults are present in both samples.

The quantitative Rietveld fit for the ordered $Cu_3Ni_2SbO_6$ sample (heated at 1345 °C) is shown in Figure 4. The high

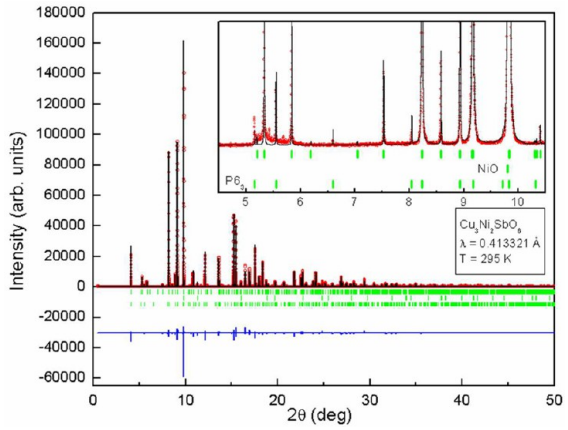

Figure 4. Quantitative structural analysis (Rietveld fit) using the high resolution synchrotron powder diffraction pattern for the ordered $Cu_3Ni_2SbO_6$ sample. Observed data (open circles), calculated model (line), and difference (lower solid line) are shown between 5° and 50° 2θ (λ = 0.413 321 Å). Bragg reflections corresponding to ordered $Cu_3Ni_2SbO_6$ (top, monoclinic *C*2/*c*), NiO (middle), and $Cu_3Ni_2SbO_6$ (bottom, hexagonal $P\bar{3}1c$) are given as tick marks below the observed data points. The insert shows the pattern between 4.5° and 11° 2θ where Bragg positions corresponding to Ni/Sb ordering are present.

intensity and resolution of the SXRD data reveals new features in the diffraction pattern. The pattern can be indexed to 3 phases: two Delafossite polytypes plus NiO. The refinement indicates the weight percentages of each phase to be 75.4(3)%, 19.9(3)%, and 4.7(1)%, respectively. The first row of hash marks in Figure 4 indicates the Bragg indices for the primary phase, a monoclinic Delafossite polytype, space group *C*2/*c* (No. 15), a = 9.194 Å, b = 5.308 Å, c = 11.917 Å, and β = 104.90°. The second row of marks indicate the Bragg positions for NiO, and the third row those of the second, 2-layer Delafossite polytype, a hexagonal unit cell, space group $P6_3$ (No. 173), $a = b$ = 5.310 Å, and c = 11.516 Å. Monoclinic unit cells are common for honeycomb-layer Delafossites and $NaFeO_2$ structures such as Cu_5SbO_6[9] and $Na_3Co_2SbO_6$.[19] Refined unit cell and atomic position parameters can be found for the primary Delafossite phase in Table 1, while the atomic distances and angles are presented in Table 2 and a depiction of the monoclinic unit cell is given in Figure 6a,b.

Figure 5 gives the quantitative Rietveld fit for $Cu_3Co_2SbO_6$. The pattern can be fitted to a single Delafossite phase, space group *C*2/*c*, a = 9.327 Å, b = 5.385 Å, c = 11.911 Å, β = 105.12°, and a $(Co,Sb)_3O_4$ spinel (space group $Fd\bar{3}m$, a = 8.53 Å); the refined weight percentages are 98.18(2)% and 1.82(2)%, respectively. Two peaks at 2θ = 11.35° (I/I_{max} = 1%) and 13.12° (I/I_{max} = 0.2%) could not be indexed to a Delafossite polytype or a known impurity phase and were omitted from the refinement. The insert in Figure 5 shows the stacking fault region between 4° and 11°; when compared to the Ni polytype there are fewer peaks present in the stacking fault region. There is one additional peak at 5.08° that may be a contribution from a second stacking polytype; however, its intensity is low (I/I_{max} = 0.3%). Other characteristic peaks corresponding to the second 2-layer polytype found in $Cu_3Ni_2SbO_6$ are absent in the ordered sample, but present in the disordered one (Figure 3).

The structure of the monoclinic Delafossite polytype determined by the quantitative Rietveld fit consists of stacked planes of metal oxygen octahedra separated by Cu^{1+} sticks, with the axes of the octahedra in neighboring planes rotated by 180° around the stacking axis (Figure 6a). This orientation of the octahedra is also that of the 2*H* polytype (Figure 6c). The stacking (coloring) of the Sb atoms when considered alone is distorted cubic close packed (ccp), with the position of the Sb atom changing across the layers in a ...ABCABC... fashion, similar to the stacking of the 3R polytype. Thus, the monoclinic cell of this honeycomb Delafossite can be related to the traditional 2*H* (structure) and 3*R* (coloring) polytypes. Note that this ordering should not be confused with the recently reported D4 polytype of $AgCoO_2$ in which the stacking type is a combination of 2*H* (structure) and 3*R* (structure) stacking.[6]

In the case of $Cu_3Ni_2SbO_6$, the powder pattern can be dimensionally fit with a hexagonal cell of $a = b$ = 5.308 Å and c = 34.549 Å, a 6-layer compound. However the hexagonal symmetry constrains the Ni and Sb to special positions; the monoclinic cell employed provides more positional degrees of freedom, which gives a better quantitative structural model fit to the data. This is also the case for $Cu_3Co_2SbO_6$ where the 6-layer hexagonal cell is $a = b$ = 5.385 Å, c = 34.495 Å. It is reasonable to expect that Ni (or Co) and Sb will have different bond lengths to oxygen and that the O−Cu^{1+}−O sticks do not need to be perfectly perpendicular to the layers of edge-sharing octahedra; these distortions are better accommodated by monoclinic symmetry than by hexagonal symmetry. It is worth noting that $Cu_3M_2SbO_6$ (M = Mn, Zn, and Mg) have been reported to have 6-layer hexagonal cells;[12] it may be that these phases can also be described with a monoclinic structure.

The powder diffraction pattern for the second Delafossite polytype present in the $Cu_3Ni_2SbO_6$ sample can be indexed to a 2-layer hexagonal unit cell, $a = b$ = 5.30959(1) Å, c = 11.516 (1) Å, space group $P6_3$; we refer to this phase as a "2*H*" polytype. The 2*H* stacking type consists of layers of edge sharing octahedra, stacked with their octahedra axes rotated by 180° on proceeding from layer to layer, with the Sb atoms in an ...ABAB... pattern, which is depicted in Figure 6c. Due to the presence of the broader diffraction peaks for this phase, the atomic positions should be considered preliminary; they are given in Table 3, while bond lengths and angles are given in Table 4.

The presence of stacking faults in both $Cu_3Ni_2SbO_6$ polytypes and in $Cu_3Co_2SbO_6$ was accommodated in the refinement models to obtain improved agreement values. To model the nature and quantity of stacking faults, mixed Co or Ni and Sb occupancies were refined on each site. In this approach, mixed site occupancy does not represent two atoms randomly occupying the same atomic position in a layer, but rather that the average electron density at that position is best represented by a mixture from two atoms due to averaging over stacking faults. For example the mixed Ni/Sb occupancy on a Ni site (see M in Table 1 and footnote for Ni/Sb occupancy) gives a measure of how many Sb atoms are present at the Ni site in the unit cell due to a shift in the adjacent metal oxide

dx.doi.org/10.1021/ic400415h | *Inorg. Chem.* XXXX, XXX, XXX−XXX

Table 1. Crystallographic Data for Ordered $Cu_3Ni_2SbO_6$ and $Cu_3Co_2SbO_6$ Collected at 295 K with Synchrotron Radiation λ = 0.413 321 Å Includes Lattice Parameters, Atomic Positions, Refined Debye–Waller Factor (B_{ov})

				$Cu_3Ni_2SbO_6$[a]	$Cu_3Co_2SbO_6$[b]
space group				*C*2/*c* (No. 15)	*C*2/*c* (No. 15)
a (Å)				9.192 140(7)	9.327 434(13)
b (Å)				5.309 008(4)	5.385 312(7)
c (Å)				11.915 530(6)	11.911 454(11)
β (deg)				104.875 05(7)	105.132 73(19)
V (Å^3)				562.0	577.6
M1[c]	Ni^{2+}/Co^{2+}	8*f*: *x*, *y*, *z*	*x*	0.0824(1)	0.0833(2)
			y	0.2494(2)	0.2497(2)
			z	0.4995(1)	0.4997(1)
M2[c]	Sb^{5+}	4*c*: $^3/_4$, $^3/_4$,0			
Cu1	Cu^{1+}	8*f*: *x*, *y*, *z*	*x*	0.8251(1)	0.8233(1)
			y	0.0909(2)	0.0887(2)
			z	0.2492(1)	0.2497(2)
Cu2	Cu^{1+}	4*e*: 0, *y*,$^1/_4$	*y*	0.5854(3)	0.5877(3)
O1	O^{2-}	8*f*: *x*, *y*, *z*	*x*	0.6191(5)	0.6244(7)
			y	0.5888(9)	0.5938(11)
			z	0.0914(5)	0.0912(6)
O2	O^{2-}	8*f*: *x*, *y*, *z*	*x*	0.7233(5)	0.7207(7)
			y	0.5764(9)	0.5702(11)
			z	0.4088(5)	0.4105(6)
O3	O^{2-}	8*f*: *x*, *y*, *z*	*x*	0.4396(5)	0.4422(7)
			y	0.0825(9)	0.0849(11)
			z	0.0882(5)	0.0879(6)
B_{ov} (Å^2)				0.245(3)	0.666(3)
R_{Bragg} (%)				6.58	6.25
R_p (%)				15.8	14.7
wR_p (%)				18.2	16.4
χ^2				7.764	8.09

[a]Synthesized at 1345 °C. [b]Synthesized at 1250 °C. [c]$Cu_3Ni_2SbO_6$ occupancies for M1–Ni/Sb 0.8930(9)/0.1070(9), M2–Ni/Sb 0.2140(9)/0.7860(9), $Cu_3Co_2SbO_6$ occupancies for M1–Co/Sb 0.8803(9)/0.1198(9), M2–Co/Sb 0.2395(9)/0.7608(9); Sb1 and Ni2/Co2 occupancies have been constrained to a 1-to-2 ratio.

plane that is not along a unit cell vector (i.e., a stacking fault). The freely refined ratios of Ni on the Sb site and Sb on the Ni site are very close to 2:1, as expected for stacking faults, and thus were fixed to this ratio using a constraint in the final refinements. (The 2 to 1 ratio is representative of the ratio of Ni/Co to Sb in the honeycomb structure and is expected to be maintained in the presence of stacking faults.) The refined M:Sb ratios imply an ~11% stacking disorder for $Cu_3Ni_2SbO_6$ and ~12% for $Cu_3Co_2SbO_6$ in the ordered variants.

Bond lengths and angles between the metal atoms and oxygens are of interest for understanding the magnetic coupling within the honeycomb lattice; Table 2 lists them. Comparison of the $Cu_3Ni_2SbO_6$ and $Cu_3Co_2SbO_6$ monoclinic structures reveals subtle differences. The in-plane *a* and *b* axes of $Cu_3Co_2SbO_6$ are ~0.13 and 0.08 Å larger than those in $Cu_3Ni_2SbO_6$, while the interlayer spacing is essentially unchanged, being only slightly smaller, by 0.009 Å. The size difference for the *ab* plane can be understood by the longer M–O bond lengths in the metal-oxide octahedral layer for $Cu_3Co_2SbO_6$, av = 2.10(2) Å compared to that of $Cu_3Ni_2SbO_6$, av = 2.07(2) Å, while the M–O–M bond angles across the honeycomb lattice are equivalent. This results in the average distance between magnetic atoms in the honeycomb lattice being slightly larger for $Cu_3Co_2SbO_6$, 3.109(3) Å, compared to 3.064(3) Å for $Cu_3Ni_2SbO_6$. Upon comparison of the present results to the structure of Cu_5SbO_6,[9] it is evident that these structures have a much more uniform honeycomb lattice due to the absence of the strong Jahn–Teller distortion present for Cu^{2+}.

HRTEM and SAED were used to further characterize the sample morphology; emphasis was placed on indentifying the polytypes and stacking faults present in each sample. To facilitate understanding of the SAED and HRTEM results, it is useful to recall that the basal plane of both $Cu_3Ni_2SbO_6$ and $Cu_3Co_2SbO_6$, space group *C*2/*c*, is pseudohexagonal and can satisfactorily be modeled in space group $R\bar{3}$. Therefore, projections of the structure along $[100]_m$, $[130]_m$, and $[-130]_m$ lead to equivalent results, as do projections along $[110]_m$, $[010]_m$, and $[-110]_m$ (the subscript *m* denotes monoclinic). Translation of the zone axes to the 4-index notation of a pseudohexagonal unit cell gives $[1-100]_h$, $[10-10]_h$, and $[01-10]_h$ and $[2-1-10]_h$, $[11-20]_h$, and $[-1-120]_h$ (the subscript *h* denotes hexagonal), respectively. This implies that the zone axes suitable for detecting any stacking disorder that may be present, i.e., those of $[100]_m$ and of $[010]_m$ types, are separated by 30° tilts in the same microcrystallite (i.e., $[1-100]_h$ into $[2-1-10]_h$, respectively). In addition to the crystallographic characterization, described below, we point out that $Cu_3Ni_2SbO_6$ shows similar, but more pronounced defect phenomena in SAED and HRTEM than $Cu_3Co_2SbO_6$. In addition, the $Cu_3Co_2SbO_6$ sample contains an additional spinel phase, Co_5SbO_8, also noted in the synchrotron powder diffraction (Figure 5) and magnetic susceptibility (Figure 13), that was easily identified by SAED and EDXS. $Cu_3Ni_2SbO_6$ is

dx.doi.org/10.1021/ic400415h | Inorg. Chem. XXXX, XXX, XXX–XXX

Table 2. Bond Distances (Å) and Angles (deg) for Ordered $Cu_3Ni_2SbO_6$ and $Cu_3Co_2SbO_6$ Determined by Rietveld Refinement at 295 K

		$Cu_3Ni_2SbO_6$[a]	$Cu_3Co_2SbO_6$[b]
M	*d* M−O1	2.074(4)	2.130(6)
		2.085(5)	2.131(6)
	d M−O2	2.058(5)	2.099(6)
		2.099(6)	2.101(7)
	d M−O3	2.038(5)	2.067(6)
		2.085(5)	2.086(7)
	d_{av}	2.07(1)	2.10(2)
	ΘO1−M−O2	177.3(4)	175.5(5)
	ΘO1−M−O3	176.5(4)	176.4(5)
	ΘO2−M−O3	179.1(5)	177.8(6)
	Θ_{av}	176.6(8)	176.6(9)
	d_{hc1}, d_{hc2}, d_{hc3}	3.052(2), 3.063(2), 3.078(2)	3.107(2), 3.113(2), 3.107(2)
	Θ_{hc1}, Θ_{hc2}, Θ_{hc3}	94.4(2), 96.0(2) 95.5(2)	93.7(3), 97.0(3), 95.4(3)
	*d*hc layer	5.746(1)	5.741(1)
Sb	*d* Sb−O1	2.010(6) × 2	1.981(7) × 2
	d Sb−O2	2.026(5) × 2	2.008(6) × 2
	d Sb−O3	1.998(4) × 2	2.030(6) × 2
	d_{av}	2.01(2)	2.01(2)
	ΘO1−Sb−O1	180.0(5)	180.0(7)
	ΘO2−Sb−O2	180.0(5)	180.0(6)
	ΘO3−Sb−O3	180.0(4)	180.0(5)
Cu	ΘO−Cu−O	176.6(6), 179.1(4)	176.4(7), 179.1(6)

[a]Synthesized at 1345 °C. [b]Synthesized at 1250 °C.

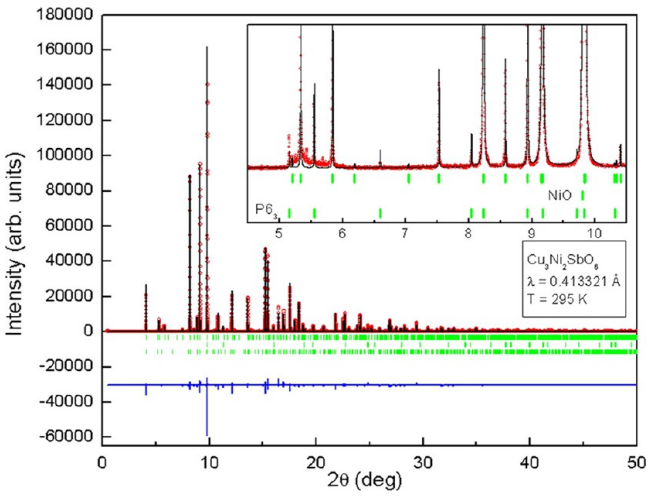

Figure 5. Quantitative structural analysis (Rietveld fit) using the high resolution synchrotron powder X-ray diffraction pattern of the ordered $Cu_3Co_2SbO_6$ sample. Observed data (open circles), calculated model (line), and difference (lower solid line) are shown between 5° and 50° 2θ (λ = 0.413 321 Å). Bragg reflections corresponding to ordered $Cu_3Co_2SbO_6$ (top) and $Co_7Sb_2O_{12}$ spinel (bottom) are given as tick marks below the observed data points. The insert shows the pattern between 4.5° and 11° 2θ where Bragg positions corresponding to Co/Sb ordering are present.

more stable to electron beam damage than $Cu_3Co_2SbO_6$; thus, the images included here were recorded for $Cu_3Ni_2SbO_6$.

In all cases the Delafossite polytypes of $Cu_3Ni_2SbO_6$ and $Cu_3Co_2SbO_6$ under consideration do not exhibit differences in the stacking of their Cu and mixed Ni/Sb or Co/Sb honeycomb layers. The axes of the metal octahedra are rotated

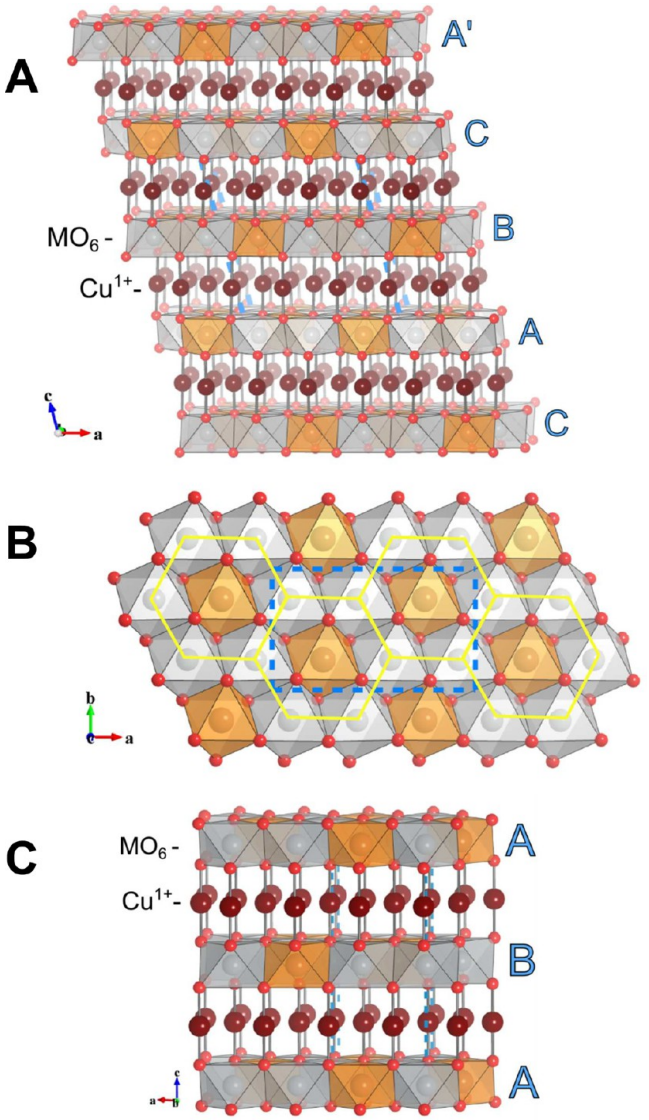

Figure 6. (a) Depiction of the honeycomb Delafossite structure, space group *C*2/*c*. Cu^{1+} sticks are shown as red spheres separating metal oxide Ni_2SbO_6 or Co_2SbO_6 layers. Metal (Ni or Co) and Sb octahedra are depicted in silver and orange respectively (color online). (b) View along the *ab* metal oxide plane with honeycomb ordering and monoclinic unit cell. (c) Depiction of the secondary 2*H* polytype.

by 180° from one layer to the next, in agreement with the Rietveld models discussed above. During examination of crystals in the $[100]_m$ orientation, the polytypes cannot be differentiated by SAED and HRTEM. Figure 7 a,b shows the corresponding SAED pattern in $[100]_m$ type crystal orientation, indicating ideal crystallinity in the aberration-corrected HRTEM image in unsurpassed resolution: even the oxygen atoms coordinating the Cu layers in a stick-like configuration are observed (Figure 7b). Tilting this microcrystallite by 30° into a zone axis of $[010]_m$ type reveals the existence of stacking faults, either as isolated or consecutive planes. These stacking faults do not involve layer reorientations,[20] but rather, within the general layer sequence, the shift of the layers to move the one metal (i.e., Ni) to a position where the other (i.e., Sb) would normally be expected: the "decoration" or "coloring" of the layers is altered in the stacking faults. Figure 8a shows a

dx.doi.org/10.1021/ic400415h | Inorg. Chem. XXXX, XXX, XXX−XXX

Table 3. Structural Data for the 2-Layer Hexagonal "2*H*" Polytype of $Cu_3Ni_2SbO_6$

				$Cu_3Ni_2SbO_6$ (1345 °C)
space group				$P6_3$ (No. 173)
a (Å)				5.309 59(1)
c (Å)				11.516(1)
V (Å^3)				
Ni1[a]	Ni^{2+}	4*f*: $^1/_3$, $^2/_3$, *z*	*z*	0.0001(1)
Ni2[a]	Ni^{2+}	2*a*: 0, 0, $^1/_4$		
Ni3[a]	Ni^{2+}	2*d*: $^2/_3$, $^1/_3$, $^1/_4$		
Ni4[a]	Ni^{2+}	2*c*: $^1/_3$, $^2/_3$, $^1/_4$		
Sb5[a]	Sb^{5+}	2*b*: 0, 0, 0		
Cu1	Cu^{1+}	12*i*: *x*, *y*, *z*	*x*	0.3218(2)
			y	0.3304(2)
			z	0.1258(1)
O1	O^{2-}	12*i*: *x*, *y*, *z*	*x*	0.3226(1)
			y	0.327(1)
			z	0.0451(3)
O2	O^{2-}	12*i*: *x*, *y*, *z*	*x*	0.3344(9)
			y	0.337(1)
			z	0.2050(3)

[a]Occupancies Ni/Sb: Ni1 − 0.728(4)/0.272(4), Ni2 − 0.755(6)/0.245(6), Ni3 − 0.607(1)/0.393(1), Ni4 − 0.575(6)/ 0.425(6), Sb5 − 0.488(6)/0.512(6). Total Ni/Sb = 1.94/1.06.

Table 4. Structural Data, Bond Distances (Å), and Angles (deg) for the Hexagonal "2*H*" Polytype of $Cu_3Ni_2SbO_6$ Determined by Rietveld Refinement at 295 K

		$Cu_3Ni_2SbO_6$ (1345 °C) hexagonal, $P6_3$ (No. 173)
Ni/Sb	*d* Ni1−O1	2.056(5)
		2.088(5)
	d Ni2−O2	2.061(5)
	d Ni3−O2	2.053(5)
	d Ni4−O2	2.038(5)
	d Sb1−O1	2.013(5)
	d_{av}	2.05(1)
	ΘO1−Ni1−O1	96.8(5)
	ΘO2−Ni2−O2	96.9(3)
	ΘO2−Ni3−O2	96.8(5)
	ΘO2−Ni4−O2	96.4(4)
	ΘO1−Sb1−O1	95.8(4)
	d_{hc1}, d_{hc2}, d_{hc3}	3.064(1), 3.064(1), 3.064(1)
	Θ_{hc1}, Θ_{hc2}, Θ_{hc3}	95.4(3), 96.8(2), 96.3(2), 97.0(2)
Cu	ΘO−Cu−O	178.0(7)

SAED pattern of the main, monoclinic polytype (Ramsdell symbol: 2*M*).

The pattern shows distinct streaking along [001]*, indicating the existence of stacking faults. Figure 8b is an overview dark-field image using the diffuse intensity of the streaks between two Bragg reflections. The density of the stacking faults is rather high; 10 nm may be taken as a measure of their average separation. It is possible that, within a honeycomb layer, the ordering of Sb atoms is not in phase over long distances, but rather that (2-dimensional) ordering domains are formed that are in antiphase position to each other. Then the stacking scheme would vary from place to place, and it can be understood why one stacking fault in Figure 8b does not extend over the whole image area. Astonishingly, SAED patterns did not show pronounced formation of twin domains, as may be expected for the monoclinic polytype.

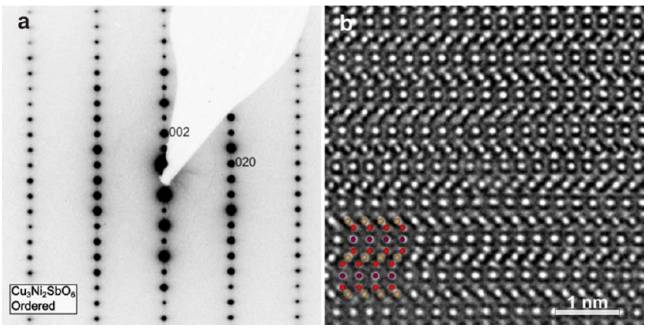

Figure 7. (a) SAED pattern in the $[100]_m$ crystal orientation of the monoclinic Ni polytype and (b) aberration-corrected HRTEM image in which columns of Ni/Sb, Cu, and O atoms are clearly resolved. The overlay in part b shows the corresponding projection of the crystal structure following the color code used in Figure 6.

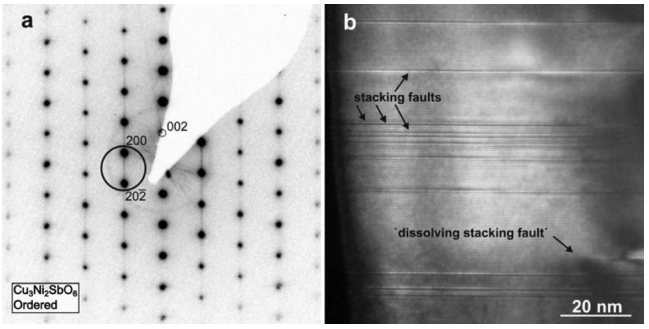

Figure 8. Stacking faults in the monoclinic Ni polytype brought in $[010]_m$ crystal orientation: (a) SAED pattern where streaking along [001]* can be observed and (b) dark-field image using the encircled two Bragg reflections with the diffuse intensity in between. Stacking faults realized as strong horizontal lines.

Figure 9 shows a rather undisturbed region of the main polytype with some stacking faults in an aberration-corrected TEM image. The Ni/Sb layer is emphasized by an appropriate choice of focus, the larger dot being Sb. A blue line has been drawn to guide the eye along the translation of the Sb atoms across the layers. An AA stacking of two neighboring Ni/Sb layers is also visible, another example of a stacking fault.

The 2*H* polytype (...ABAB... stacking), identified in the SXRD pattern of $Cu_3Ni_2SbO_6$ (Figure 4), can be observed in extended (3-dimensional) domains in Figure 10a; the primary monoclinic polytype can also be observed in this image. Both are highlighted with blue lines. These domains are large enough to generate a "single crystal" SAED pattern as shown in Figure 10b. A simulated kinematical electron diffraction pattern based on the 2*H* structural model (Table 4) is shown in Figure 10c and gives good agreement with the SAED pattern, corroborating the inclusion of the 2*H* phase in the Rietveld refinement of ordered $Cu_3Ni_2SbO_6$. The existence of many other polytypes, at least in smaller domains, may be postulated.

Figure 11 shows an exotic long-range stacking order built up of 10 layers described with Hägg symbols, where + is forward and − is back, |+ + + − + − + − + −|. Close examination of the stacking fault region (5−6° 2θ) in the SXRD patterns (Figures 3 and 4) reveals additional superstructure peaks which were not indexed by the two Ni polytypes: it is possible that they are representative of this higher order polytype. Evidence of such a large ordered cell is unexpected as very long period Delafossite polytypes are rare, but due to the presence of the other two Ni

dx.doi.org/10.1021/ic400415h | *Inorg. Chem.* XXXX, XXX, XXX−XXX

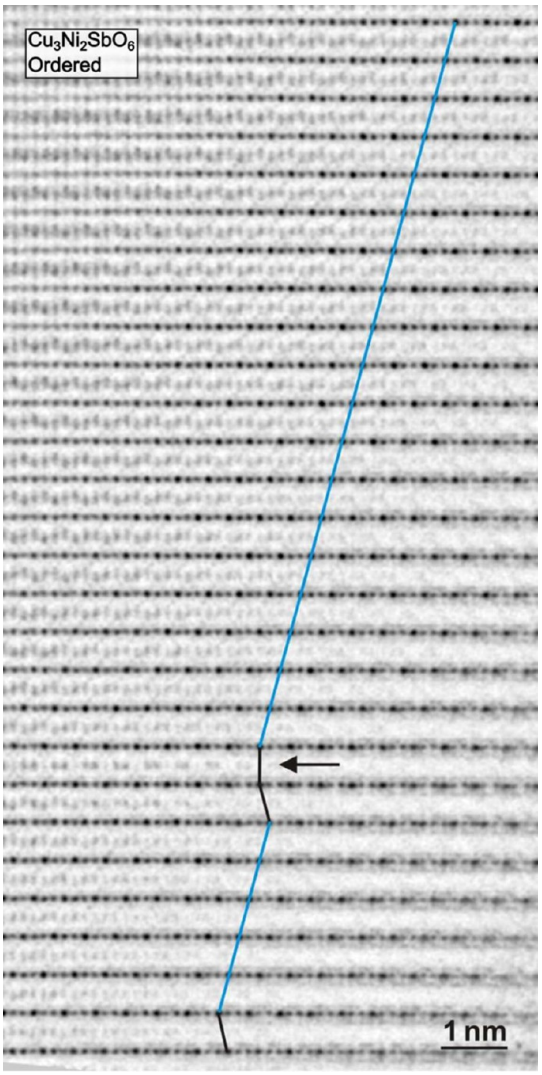

Figure 9. Aberration-corrected HRTEM image of the monoclinic Ni polytype where the primary ...ABC... coloring is highlighted with a blue line. Stacking faults are also observed as regions of discontinuity in the lower third of the image; one of them shows an AA stacking of two neighboring Ni/Sb layers. Image contrast was inverted for reproduction.

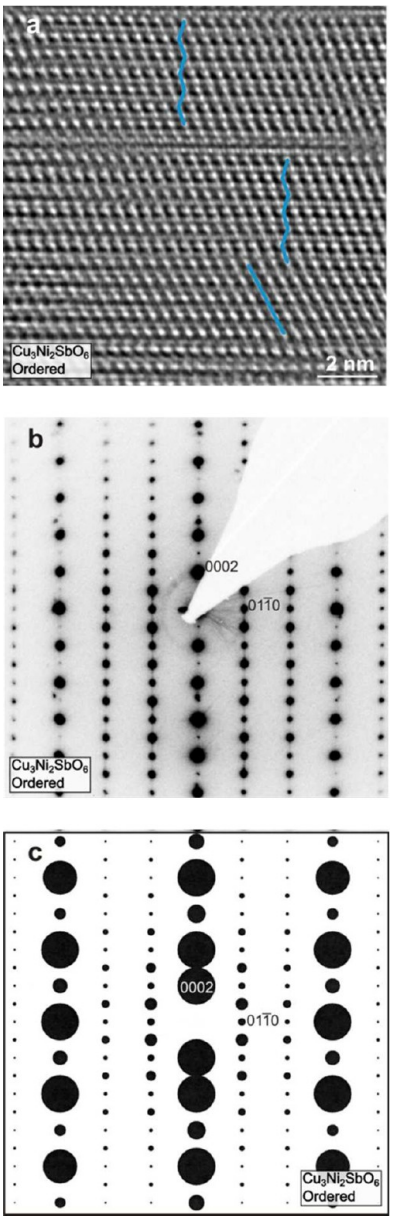

Figure 10. (a) HRTEM image of the "2*H*" polytype and (b) SAED pattern. In part a, stacking faults as well as inserted lamellae of monoclinic stacking are visible. Consequently the pattern in part b shows weak diffuse streaking along [0001]*. (c) Simulated kinematical electron diffraction pattern for the "2*H*" polytype based on the data set given in Table 3.

polytypes, quantification of this phase is beyond the scope of this work.

Magnetic Characterization. The temperature dependent magnetic susceptibilities of the ordered and disordered versions of $Cu_3Ni_2SbO_6$ and $Cu_3Co_2SbO_6$ all display a Curie–Weiss (CW)-like increase with decreasing temperature; there are no significant differences between the ordered and disordered versions of the two compounds. Accordingly, the susceptibilities of the ordered versions are presented. The data are analyzed in terms of $\chi = \chi_0 + C/(T - \theta)$, where χ_0 is a constant background contribution, C is the Curie constant, and θ the Curie–Weiss temperature.

The magnetic susceptibility of $Cu_3Ni_2SbO_6$ and its inverse are shown in Figure 12. A maximum in the susceptibility at T_N = 22.3 K signals a transition to an antiferromagnetically ordered state. The inverse susceptibility shows linearity above $T \approx 100$ K, indicating a very small χ_0. Accordingly, a least-squares analysis of the susceptibility data was performed at temperatures above 100 K. If a background contribution is included in the fit we obtain $\theta = -6.16$ K, $\mu_{eff} = 3.04\ \mu_B/(Ni^{2+})$, and $\chi_0 = 0.000\ 89\ \mu_B/(Ni^{2+})$. With χ_0 as a free parameter the goodness of the fit is improved, but significant correlations result between the lower temperature range of the fit (T_{low}), θ, and μ_{eff}. Therefore, a fixed value, $\chi_0 = 0$, was chosen, for the very small background contribution making the fitting parameters robust against the choice of temperature range for $T_{low} > 100$ K. The obtained values are $\theta = -20.5$ K, and $\mu_{eff} = 3.27\ \mu_B$. The solid line in Figure 12 is the calculated inverse susceptibility with $\chi_0 = 0$.

The susceptibility of $Cu_3Co_2SbO_6$, shown in the insert of Figure 13, reveals a rapid increase below 60 K and a peak at 18.5 K. The rapid increase below 60 K is attributed to the presence of the $(Co,Sb)_3O_4$ spinel phase observed by SXRD.

dx.doi.org/10.1021/ic400415h | *Inorg. Chem.* XXXX, XXX, XXX–XXX

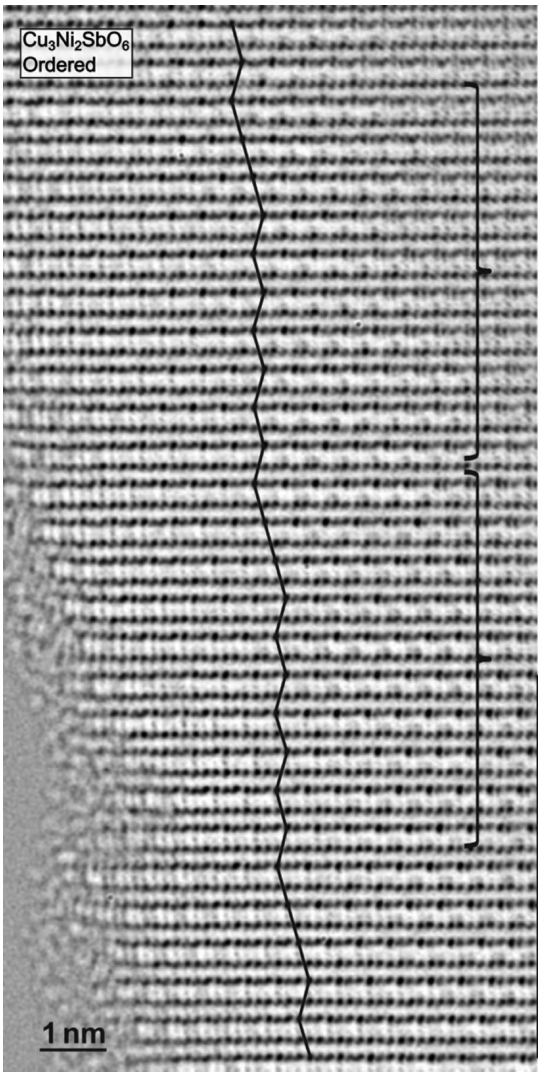

Figure 11. Aberration-corrected HRTEM image of an exotic high-order Ni polytype with a 10 layer unit indicated by brackets. The crystal is a bit out of the correct zone axis, but the stacking of the Sb atoms is clearly visible. The stacking is mainly "2*H*", interrupted regularly by lamellae of monoclnic stacking. Image contrast was inverted for reproduction.

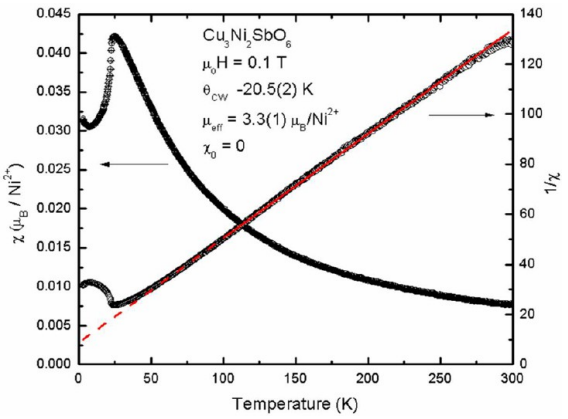

Figure 12. Magnetic susceptibility χ of $Cu_3Ni_2SbO_6$ in units of μ_B/Ni/T (open circles) and the corresponding inverse susceptibility χ^{-1} (closed circles) from 2 to 300 K measured at 0.1 T. The red line represents a Curie–Weiss fit ($\chi = C/(T - \theta)$ from T = 100–294 K, where $\theta = -20.5(2)$, and $\mu_{eff} = 3.3(1)\ \mu_B/Ni^{2+}$. The antiferromagnetic ordering temperature is T_N = 22.3 K.

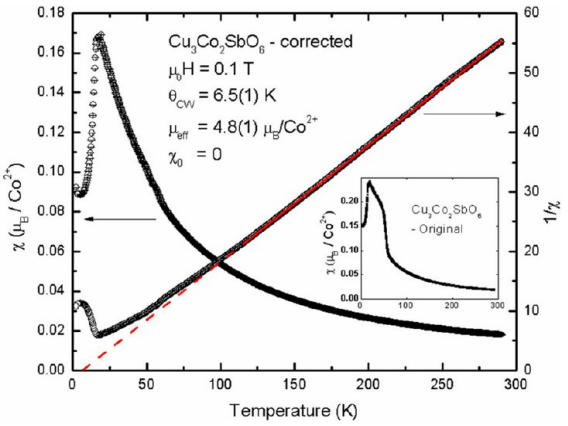

Figure 13. Magnetic susceptibility χ of $Cu_3Co_2SbO_6$ in units of μ_B/Co/T corrected for the contribution from the $(Co,Sb)_3O_4$ impurity phase (open circles) from 2 to 295 K measured at 0.1 T. The inset shows the uncorrected data. The corresponding inverse susceptibility χ^{-1} is shown as closed circles. The red line represents a Curie–Weiss fit ($\chi = C/(T - \theta)$ from T = 120 to 295 K, where $\theta = 6.5(1)$, and μ_{eff} = 4.8(1) μ_B/Co. The antiferromagnetic ordering temperature is T_N = 18.5 K.

This conclusion is based on the following observations: first, the $(Co,Sb)_3O_4$ spinel phases show different types of magnetic order below temperatures of about 60 K, depending on the Co and Sb composition.[21,22] Second, Co_5SbO_8 was synthesized, and its measured susceptibility shows features that are consistent with the ferrimagnetic ordering reported in ref 22, and with the anomalous increase in the $Cu_3Co_2SbO_6$ data (see Figure 13, insert). Third, the anomaly is far less significant in an applied field of 1 T, which indicates that the ordering is ferro- or ferrimagnetic. The anomaly has been removed by subtracting a scaled amount of the measured Co_5SbO_8 susceptibility. The scaling is performed on amplitude as well as temperature in order to obtain a smooth $Cu_3Co_2SbO_6$ susceptibility curve. Thus, the transition temperature of the spinel has been decreased by 7.7 K, and the intensity of its contribution corresponds to 3.64 wt % Co_5SbO_8, which is twice as much as the value from the SXRD analyses (1.82 wt %). Considering that the samples used for the susceptibility and the SXRD studies come from different batches and the exact Co–Sb composition of the $(Co,Sb)_3O_4$ spinel phase is not determined in the synthesized sample, the subtraction is reasonable and appropriate. The resulting susceptibility, shown in Figure 13, is analyzed in the same way as for $Cu_3Ni_2SbO_6$. The antiferromagnetic ordering temperature is T_N = 18.5 K. The inverse susceptibility is linear at temperatures above $T \approx 120$ K, indicating that χ_0 is also very small in this sample. A least-squares refinement of the susceptibility data above 120 K including χ_0 results in a CW temperature θ = 0.03 K, μ_{eff} = 4.96 μ_B, and $\chi_0 = -0.001\ 01\ \mu_B/(\text{Co-ion}_*T)$. As for $Cu_3Ni_2SbO_6$ the small value of χ_0 is neglected in the final refinement because it causes the above-mentioned correlations and uncertain parameters. The refined values with $\chi_0 = 0$ are θ = 6.53 K, μ_{eff} = 4.79 μ_B.

A limited comparison of magnetic susceptibility trends to other layered phases with the honeycomb motif is possible. $Na_3Co_2SbO_6$ displays an antiferromagnetic transition at 4.4 K with a Weiss constant of −0.8 K,[19] while $Na_3Ni_2SbO_6$ shows an

dx.doi.org/10.1021/ic400415h | *Inorg. Chem.* XXXX, XXX, XXX–XXX

antiferromagnetic transition at 16 K and a Weiss constant of +9.1 K.[23] The small Weiss constants of both these phases suggest the presence of a ferromagnetic contribution to the coupling, possibly like that involved in the magnetic structures realized in the Ni and Co samples (see below). It is difficult to make further conclusions without a detailed study of the atomic and magnetic structure of $Na_3Co_2SbO_6$ and $Na_3Ni_2SbO_6$.

For the similar $NaFeO_2$-based structure compound, $Na_3Co_2SbO_6$, the magnetic transition occurs at 4.4 K[19] suggesting that stronger coupling through the Cu^{1+} layer may play a role in the higher transition temperature for the current compounds. The observations that the linearity of χ^{-1} is only found at temperatures significantly higher than the 3D ordering temperatures in the current compounds, and similarly that the $d(M \times T)/dT$ plots shown in Figure 14 are only zero at high temperatures, suggest the presence of 2D in-plane ordering that has set in below about 100 K.

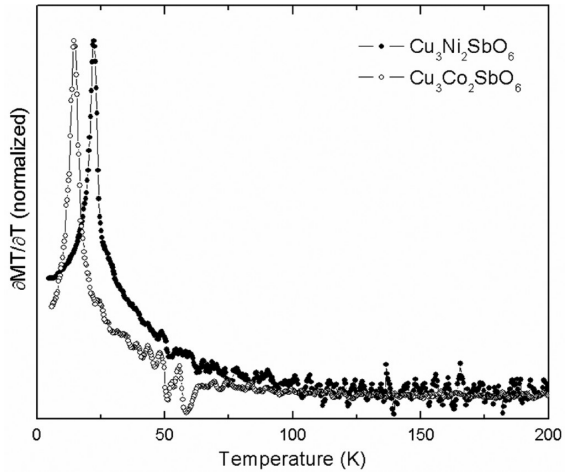

Figure 14. Normalized plot of $d(M \times T)/dT$ for $Cu_3Ni_2SbO_6$ (open circles) and $Cu_3Co_2SbO_6$ (closed circles) between 0 and 200 K. Magnetization (M) is taken as $\chi \times H$.

The Curie–Weiss fit for the $Cu_3Ni_2SbO_6$ sample gives a CW temperature of $\theta = -20.5$ K, typical of dominantly antiferromagnetic coupling and in good agreement with the magnetic ordering temperatures of $T_N = 22.3$ K. The calculated effective magnetic moment is 3.43 μ_B per Ni, which is within the typical range expected for Ni^{2+} atoms with $S = 1$. The $Cu_3Co_2SbO_6$ sample gives a CW temperature of $\theta = 6.5$ K, suggesting the existence of significant ferromagnetic couplings in this compound. The calculated effective magnetic moment is 4.8 μ_B per Co, which is quite high for $S = {}^3/_2$, but at a typical value for Co^{2+}. It is unusual that the CW temperature is significantly lower and of opposite sign than the magnetic ordering temperature $T_N = 18.5$ K for an apparently antiferromagnetic material. This observation indicates the presence of significant next nearest neighbor magnetic interactions in the $Cu_3Co_2SbO_6$ compound, of opposite sign from nearest neighbor interactions, making the observed θ values in the fitted temperature range smaller than would be found for a simple system where only near neighbor interactions are significant.

Magnetization data for both compounds as a function of applied field are given in Figure 15. For $Cu_3Ni_2SbO_6$, the magnetization is linear with applied field, typical of an antiferromagnet, while for $Cu_3Co_2SbO_6$ the magnetization

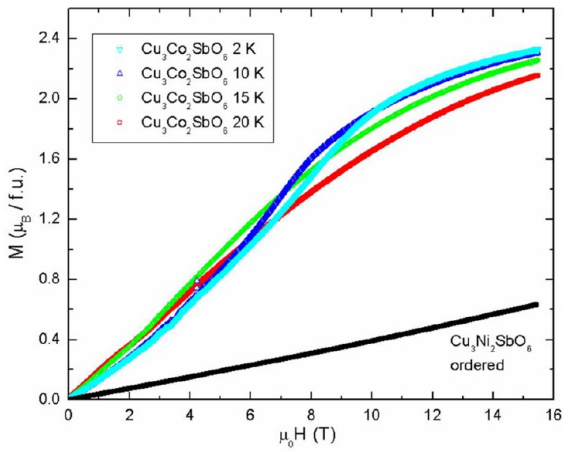

Figure 15. Plot of magnetization M (μ_B/Ni or Co atom) versus field (T) for ordered $Cu_3Ni_2SbO_6$ (closed symbols) and $Cu_3Co_2SbO_6$ (open symbols) at various temperatures between 0 and 16 T.

curves below T_N have a positive curvature (S-like shape), which suggests a more complex magnetic ordering, and a possible field induced magnetic phase transition. Detailed studies and analyses of this observation are beyond the scope of the present study.

The heat capacity of the samples has been measured from 2 to 250 K (Figure 16); the nonmagnetic analogue $Cu_3Zn_2SbO_6$

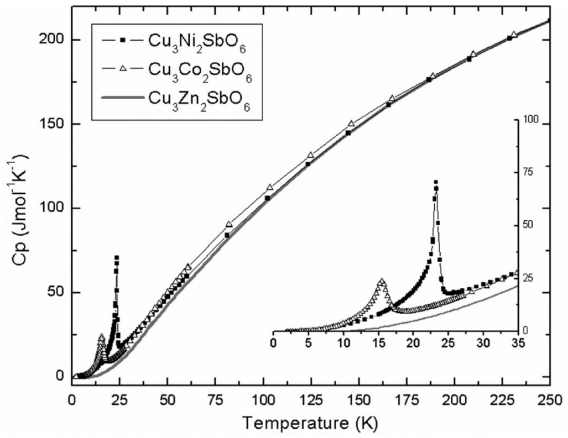

Figure 16. Heat capacity (J mol^{-1} K^{-1}) of $Cu_3Ni_2SbO_6$ (squares), $Cu_3Co_2SbO_6$ (open triangles), and nonmagnetic $Cu_3Zn_2SbO_6$ (gray line) between 2 and 250 K. The insert shows a close up of the region between 2 and 35 K.

was used to subtract the phonon contribution and obtain the magnetic specific heat for each sample. Both samples display sharp, λ-anomaly-like transitions in the magnetic specific heat at the same temperatures as their magnetic susceptibility transitions. A plot of the magnetic specific heat, Figure 17, reveals the release of latent magnetic entropy above the transition temperature, consistent with the curvature above T_N in the $d(H/M)/dT$ plots. Integration of the magnetic entropy highlights this observation. The slope of the $Cu_3Ni_2SbO_6$ sample is sharpest at 22 K, but the entropy does not saturate to the expected value ($R \ln(2S + 1)$) until ~100 K, while for the $Cu_3Co_2SbO_6$ sample there is a sharp feature at 16 K, then a gradual increase to ~150 K, where the magnetic specific heat saturates.

dx.doi.org/10.1021/ic400415h | Inorg. Chem. XXXX, XXX, XXX–XXX

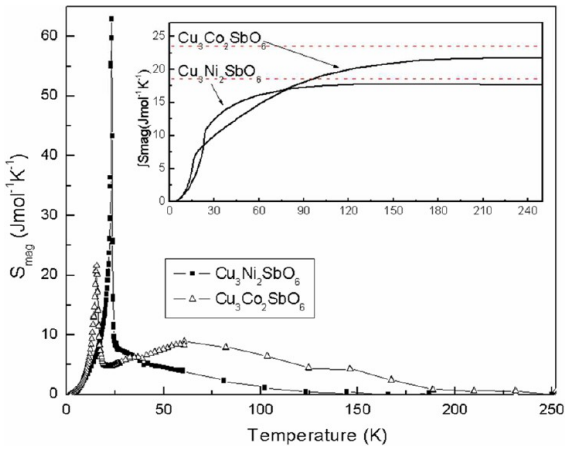

Figure 17. Magnetic heat capacity of $Cu_3Ni_2SbO_6$ (squares) and $Cu_3Co_2SbO_6$ (open triangles), obtained by subtracting the heat capacity of nonmagnetic $Cu_3Zn_2SbO_6$. The insert shows the integration of the magnetic heat capacity over the temperature range. Dotted line represent the expected entropy released per magnetic ion calculated using the equation $R \ln(2S + 1)$.

Low temperature neutron powder diffraction data (λ = 2.41 Å) are presented in Figures 18 and 19 for ordered $Cu_3Ni_2SbO_6$

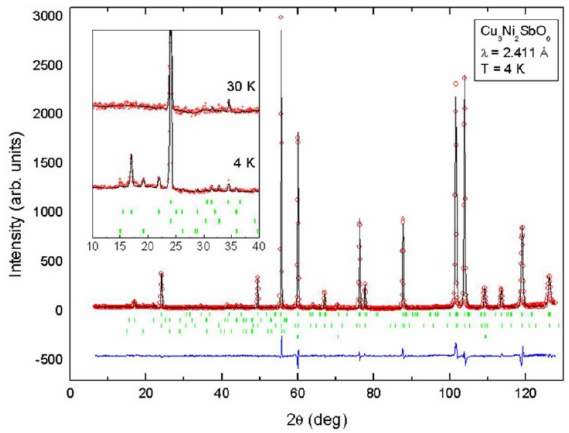

Figure 18. Magnetic structural analysis (Rietveld fit) of ordered $Cu_3Ni_2SbO_6$ using neutron powder diffraction. Observed data (open circles), calculated model (line), and difference (lower solid line) are shown between 5.5° and 126° 2θ (λ = 2.410 879 Å). Bragg reflections corresponding to ordered $Cu_3Ni_2SbO_6$ atomic structure (top), magnetic structure (middle), and NiO (bottom) are given as tick marks below the observed data. The insert shows the magnetic portion of the pattern between 10° and 40° 2θ with overlays of spectra taken at 15 and 30 K.

and $Cu_3Co_2SbO_6$, respectively. At 4 K both compounds show the appearance of new peaks due to the ordering of magnetic spins that are absent in the patterns collected above their transition temperatures (see inserts). For both $Cu_3Ni_2SbO_6$ and $Cu_3Co_2SbO_6$ the magnetic peaks can be indexed to a magnetic propagation vector $\mathbf{k} = [100]$.

The magnetic models that best fit the data were defined in the frame of basis vectors ψ1and ψ3 of the IR Γ1 for the case of Ni, and ψ8 of the Γ3 for Co (see Table 5). Overall, the magnetic structures can be described as ferromagnetic chains along the *b* direction which are antiferromagnetically coupled to their neighboring chains, resulting in an overall antiferromagnetic "zigzag" ordering in the honeycomb plane, as

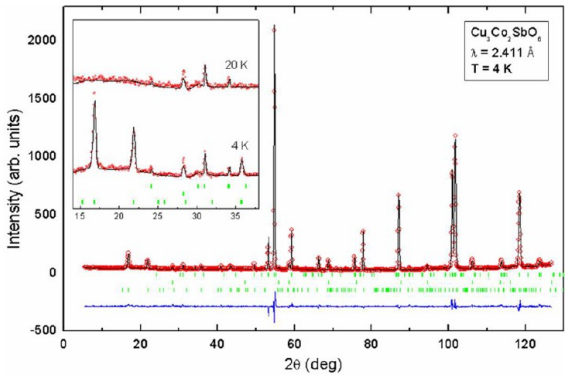

Figure 19. Magnetic structural analysis (Rietveld fit) of ordered $Cu_3Co_2SbO_6$ using neutron powder diffraction. Observed data (open circles), calculated model (line), and difference (lower solid line) are shown between 5.5° and 126° 2θ (λ = 2.410 879 Å). Bragg reflections corresponding to ordered $Cu_3Co_2SbO_6$ atomic structure (top), $Co_7Sb_2O_{12}$ spinel (middle), and magnetic structure (bottom) are given as tick marks below the observed data. The insert shows the magnetic portion of the pattern between 14° and 38° 2θ with overlays of spectra taken at 20 K.

depicted in Figure 20. The ferromagnetic chains resemble the ordering observed in the honeycomb structure $BaNi_2(AsO_4)_2$ $\mathbf{k} = [{}^1/_2\ 0\ {}^1/_2]$.[11] Interestingly, the orientation of the magnetic moment appears to be different for the two studied compounds. While in the Co compound the moments are aligned parallel to the *b*-axis direction, in the Ni compound the moments are confined to the *ac* plane and are pointing almost perpendicular to the honeycomb planes.

This difference in magnetic moment orientation can offer an explanation for the observed differences in the bulk magnetic measurements. The Curie–Weiss fits for the Ni compound gave a negative Weiss constant, in line with the observed antiferromagnetic transition; however, the Co compound gave a positive Weiss constant, indicating the presence of significant ferromagnetic coupling. The magnetic structure in the Ni compound suggests that the ferromagnetic chains, in addition to being coupled antiferromagnetically to each other, are coupled antiferromagnetically to the chains in adjacent layers. For the Co compound the antiferromagnetic coupling between layers appears to be minimal or absent. This difference between magnetic structures is also reflected in the magnetization versus applied field measurements: the Ni compound displays classic antiferromagnetic behavior, while the Co compound has positive curvature with an S-like shape.

As discussed in the structure section, the Ni compound exhibits a second polytype ("2*H*") characterized by the hexagonal space group $P6_3$. The presence of the secondary phase is apparent in the neutron experiment through the presence of additional magnetic peaks indexed by a propagation vector $\mathbf{k} = ({}^1/_2, 0, 0)$ with respect to the 2*H* hexagonal lattice. Refinement of the neutron data yields a weight percentage of the second polytype of approximately 19%, in good agreement with the X-ray study. The magnetic structure is identical to the main polytype, which is best described as antiferromagnetic Ni layers with the direction of the moment parallel to the staking direction. The observation of the same spin structure for both polytypes is consistent with the sharp transitions observed in the magnetic susceptibility and specific heat.

The magnitudes of the ordered magnetic moments derived from the neutron diffraction data at 4 K are 1.5(1) μ_B/Ni (mx =

dx.doi.org/10.1021/ic400415h | Inorg. Chem. XXXX, XXX, XXX–XXX

Table 5. Irreproducible Representations (IRs) and Basis Vectors (BVs) for the Space Group $C2/c$ with k = (1, 0, 0)[a]

		atom (ma, mb, mc)											
IR	BV	1			2			3			4		
Γ1	ψ1	1	0	0	−1	0	0	1	0	0	−1	0	0
	ψ2	0	1	0	0	1	0	0	1	0	0	1	0
	ψ3	0	0	1	0	0	−1	0	0	1	0	0	−1
Γ2	ψ4	1	0	0	−1	0	0	−1	0	0	1	0	0
	ψ5	0	1	0	0	1	0	0	−1	0	0	−1	0
	ψ6	0	0	1	0	0	−1	0	0	−1	0	0	1
Γ3	ψ7	1	0	0	1	0	0	1	0	0	1	0	0
	ψ8	0	1	0	0	−1	0	0	1	0	0	−1	0
	ψ9	0	0	1	0	0	1	0	0	1	0	0	1
Γ4	ψ10	1	0	0	1	0	0	−1	0	0	−1	0	0
	ψ11	0	1	0	0	−1	0	0	−1	0	0	1	0
	ψ12	0	0	1	0	0	1	0	0	−1	0	0	−1

[a]The atoms of the nonprimitive basis (M= Co or Ni) are defined according to the following: 1 (x = 0.082, y = 0.249, z = 0.499), 2 ($-x + 1$, y, $-z + {}^1/_2$), 3 ($-x + 1$, $-y + 1$, $-z + 1$), 4 (x, $-y + 1$, $z + {}^1/_2$).

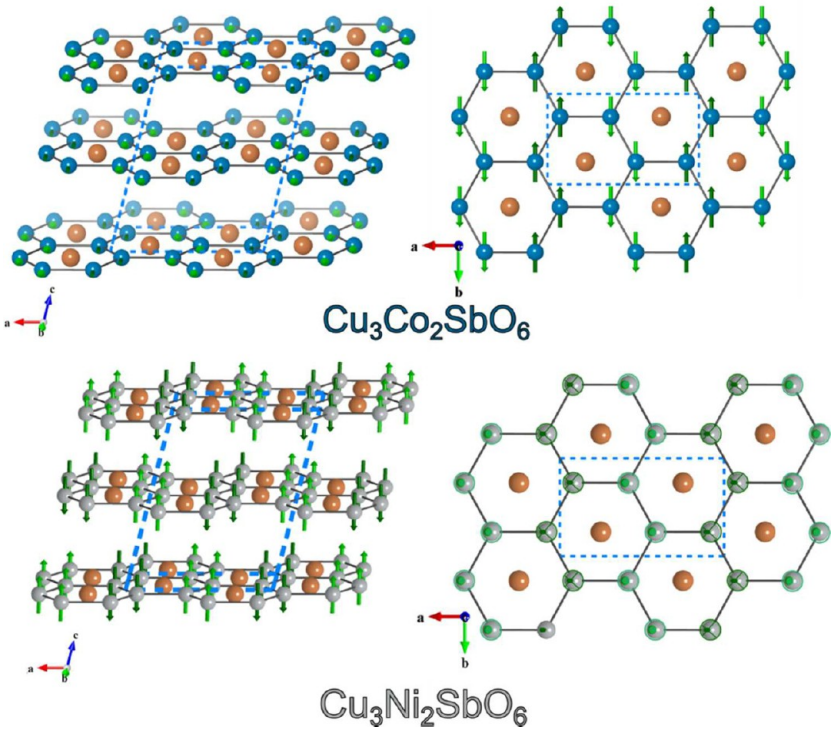

Figure 20. Magnetic structure of $Cu_3Co_2SbO_6$ (top) and $Cu_3Ni_2SbO_6$ (bottom). Both structures consist of alternating ferromagnetic chains, with the spins aligned along the b-axis for $Cu_3Co_2SbO_6$ and in the ac-plane for $Cu_3Ni_2SbO_6$.

0.44(6) and mz = 1.49(4)) for the monoclinic $Cu_3Ni_2SbO_6$ polytype, 1.9(2) μ_B/Ni for the "2H" $Cu_3Ni_2SbO_6$ polytype, and 2.4 (1)μ_B/Co for $Cu_3Co_2SbO_6$. The magnitude of the magnetic moment for both Ni and Co in the monoclinc polytypes is smaller than the expected moment for Ni^{2+} (S = 1) and Co^{2+} (S = ${}^3/_2$). It is worth noting that with our diffraction measurements we are only able to detect the static component of the magnetic moment, and the presence of strong fluctuation will result in a decrease of its value. An additional explanation for the smaller-than-expected moments is the presence of stacking faults. Each fault disrupts the magnetic coupling between adjacent layers, acting as a "glassy" component which does not contribute to the intensity of the magnetic peaks; thus, the magnitudes are lower than expected.

To evaluate the character of the long-range-order transition, the critical exponent β associated with the magnetic order parameter was measured, where β is defined as $M(T) \propto \sqrt{I} \propto (T_N - T)^{\beta}$, and plotted in Figure 21. We found that, near the transition temperatures (T_N), for both Ni and Co compounds, the evolution with the temperature of the magnetic peak (−101) is well described by an exponent β = 0.23, characteristic for the finite-size 2D XY model.[24]

CONCLUSIONS

We have reported the structure and magnetic properties of the Delafossite compounds $Cu_3Ni_2SbO_6$ and $Cu_3Co_2SbO_6$. As the samples are heated to near their melting points, additional powder diffraction peaks appear that are indexed to an ordered monoclinic unit cell in which magnetic atoms are arranged in a

dx.doi.org/10.1021/ic400415h | Inorg. Chem. XXXX, XXX, XXX−XXX

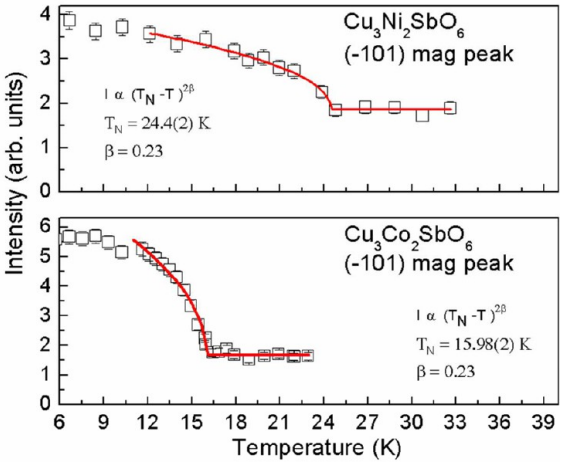

Figure 21. Plot of magnetic ordering parameter for $Cu_3Ni_2SbO_6$ (−101) peak (upper panel) and $Cu_3Co_2SbO_6$ (−101) peak (lower panel). Fits to the data are given as red lines.

honeycomb pattern. Rietveld refinement of the ordered samples using high resolution synchrotron powder diffraction confirms the honeycomb structure and reveals that the Ni sample contains two ordered polytypes, while the Co sample only contains one. In addition, the peak widths are selectively broadened for both samples, indicating the presence of stacking faults (common to Delafossites). High-resolution electron microscopy confirms the structures modeled from the Rietveld refinements as well as showing the presence of stacking faults. Magnetic susceptibility measurements indicate that the samples are both antiferromagnets, with T_N = 22.3 and 18.5 °C for the Ni and Co samples, respectively, with Curie−Weiss fits that are in agreement with Ni^{2+} and Co^{2+} high spins. Magnetization versus applied field plots are linear for the Ni sample, while the Co sample displays more complex behavior. Magnetic structures of the monoclinic polytypes were determined by neutron diffraction at 4 K. The magnetic **k** vector is [100] for both samples; however, the moments are aligned along the *b*-axis for the Co sample while for the Ni sample the moments are in the *ac* plane. The evolution of the magnetic (−101) peak was monitored, and the critical exponent β was found to be 0.23, characteristic of a 2D XY magnetic model of finite size. These compounds reflect both the structural and magnetic richness of layered honeycomb compounds of the late 3d transition elements.

■ ASSOCIATED CONTENT

Supporting Information

Crystallographic data in CIF format. This material is available free of charge via the Internet at http://pubs.acs.org.

■ AUTHOR INFORMATION

Corresponding Author

*E-mail: jhr@princeton.edu.

Notes

The authors declare no competing financial interest.

■ ACKNOWLEDGMENTS

Research at Princeton University was supported through the Department of Energy, Division of Basic Energy Sciences, Grant DOE DE-FG02-08ER46544, through The Institute for Quantum Matter at Johns Hopkins University. Use of the Advanced Photon Source at Argonne National Laboratory was supported by the U.S. Department of Energy, Office of Basic Energy Sciences, under Contract DE-AC02-06CH11357. The authors thank beamline scientists M. Suchomel, L. Ribaud, and B. Toby for the very high quality diffraction data. The research at Oak Ridge National Laboratory's High Flux Isotope Reactor was sponsored by the Scientific User Facilities Division, Office of Basic Energy Sciences, U.S. Department of Energy. R.J.C. gratefully acknowledges the support for his work at Risø DTU by the Velux Visiting Professor Program 2009-2010, and for his work at the MPI in Dresden by the Humboldt Foundation.

■ REFERENCES

(1) Kawazoe, H.; Yasukawa, M.; Hyodo, H.; Kurita, M.; Yanagi, H.; Hosono, H. *Nature* **1997**, *389*, 939−942.
(2) Lee, M.; Viciu, L.; Li, L.; Wang, Y.; Foo, M. L.; Watauchi, S.; Pascal, R. A., Jr.; Cava, R. J.; Ong, N. P. *Nat. Mater.* **2006**, *5*, 537−540.
(3) Schaak, R. E.; Klimczuk, T.; Foo, M. L.; Cava, R. J. *Nature* **2003**, *424*, 527−529.
(4) Kimura, T.; Lashley, J. C.; Ramirez, A. P. *Phys. Rev. B* **2006**, 73.
(5) Berthelot, R.; Pollet, M.; Doumerc, J. P.; Delmas, C. *Inorg. Chem.* **2011**, *50*, 6649−6655.
(6) Berthelot, R.; Pollet, M.; Doumerc, J. P.; Delmas, C. *Inorg. Chem.* **2011**, *50*, 4529−4536.
(7) Choi, S. K.; Coldea, R.; Kolmogorov, A. N.; Lancaster, T.; Mazin, I. I.; Blundell, S. J.; Radaelli, P. G.; Singh, Y.; Gegenwart, P.; Choi, K. R.; Cheong, S. W.; Baker, P. J.; Stock, C.; Taylor, J. *Phys. Rev. Lett.* **2012**, *108*, 127204.
(8) Chaloupka, J.; Jackeli, G.; Khaliullin, G. *Phys. Rev. Lett.* **2010**, *105*, 027204.
(9) Climent-Pascual, E.; Norby, P.; Andersen, N. H.; Stephens, P. W.; Zandbergen, H. W.; Larsen, J.; Cava, R. J. *Inorg. Chem.* **2012**, *51*, 557−565.
(10) Miura, Y.; Hirai, R.; Kobayashi, Y.; Sato, M. *J. Phys. Soc. Jpn.* **2006**, 75.
(11) Regnault, L. P.; Rossat-Mignod, J. Phase Transitions in Quasi Two-Dimensional Planar Magnets. In *Magnetic Properties of Layered Transition Metal Compounds*; De Jongh, L. J., Ed.; Kluwer Academic Publishers: Dordrecht, The Netherlands, 1990; pp 271−321.
(12) Nagarajan, R.; Uma, S.; Jayaraj, M. K.; Tate, J.; Sleight, A. W. *Solid State Sci.* **2002**, *4*, 787−792.
(13) Rodriguez Carvajal, J. *Phys. B* **1993**, *192*, 55−69.
(14) Uhlemann, S.; Haider, M. *Ultramicroscopy* **1998**, *72*, 109−119.
(15) Wills, A. S. *Phys. B* **2000**, *276−278*, 680−681.
(16) Momma, K.; Izumi, F. *J. Appl. Crystallogr.* **2011**, *44*, 1272−1276.
(17) Cava, R. J.; Zandbergen, H. W.; Ramirez, A. P.; Takagi, H.; Chen, C. T.; Krajewski, J. J.; Peck, W. F.; Waszczak, J. V.; Meigs, G.; Roth, R. S.; Schneemeyer, L. F. *J. Solid State Chem.* **1993**, *104*, 437−452.
(18) Todorova, V.; Leineweber, A.; Kienle, L.; Duppel, V.; Jansen, M. *J. Solid State Chem.* **2011**, *184*, 1112−1119.
(19) Viciu, L.; Huang, Q.; Morosan, E.; Zandbergen, H. W.; Greenbaum, N. I.; McQueen, T.; Cava, R. J. *J. Solid State Chem.* **2007**, *180*, 1060−1067.
(20) Ďurovič, S.; Krishna, P.; Pandey, D. *Layer Stacking, Int. Tables Crystallogr.* **2006**, *C*, 752−773.
(21) Brito, M. S. L.; Escote, M. T.; Santos, C. O. P.; Lisboa, P. N.; Leite, E. R.; Oliveira, J. B. L.; Gama, L.; Longo, E. *Mater. Chem. Phys.* **2004**, *88*, 404−409.
(22) Antic, B.; Rodic, D.; Tellgren, R.; Rundlof, H. *J. Magn. Magn. Mater.* **2000**, *219*, 41−44.
(23) Roudebush, J. H.; Cava, R. J. *J. Solid State Chem.* **2013**, submitted.
(24) Bramwell, S. T.; Holdsworth, P. C. W. *J. Phys.: Condens. Matter* **1993**, *5*, L53.

dx.doi.org/10.1021/ic400415h | *Inorg. Chem.* XXXX, XXX, XXX−XXX